AD_____

Award Number: DAMD17-99-1-9251

TITLE: Rapid, High Resolution 3-D Ultrasound Tomography

PRINCIPAL INVESTIGATOR: Jeffrey S. Kallman, Ph.D.

CONTRACTING ORGANIZATION: Lawrence Livermore National Laboratory
                           Livermore, California 94550

REPORT DATE: September 2001

TYPE OF REPORT: Final

PREPARED FOR: U.S. Army Medical Research and Materiel Command
               Fort Detrick, Maryland 21702-5012

DISTRIBUTION STATEMENT: Approved for Public Release;
                        Distribution Unlimited

The views, opinions and/or findings contained in this report are
those of the author(s) and should not be construed as an official
Department of the Army position, policy or decision unless so
designated by other documentation.

20020909 087

REPORT DOCUMENTATION PAGE

Public reporting burden for this collection of information is estimated to average 1 hour per response, including the time for reviewing instructions, searching existing data sources, gathering and maintaining the data needed, and completing and reviewing this collection of information. Send comments regarding this burden estimate or any other aspect of this collection of information, including suggestions for reducing this burden to Washington Headquarters Services, Directorate for Information Operations and Reports, 1215 Jefferson Davis Highway, Suite 1204, Arlington, VA 22202-4302, and to the Office of Management and Budget, Paperwork Reduction Project (0704-0188), Washington, DC 20503

1. AGENCY USE ONLY (Leave blank)	2. REPORT DATE September 2001	3. REPORT TYPE AND DATES COVERED Final (1 Sep 99 – 31 Aug 01)

4. TITLE AND SUBTITLE
Rapid, High Resolution 3-D Ultrasound Tomography

5. FUNDING NUMBERS
DAMD17-99-1-9251

6. AUTHOR(S)
Jeffrey S. Kallman, Ph.D.

7. PERFORMING ORGANIZATION NAME(S) AND ADDRESS(ES)
Lawrence Livermore National Laboratory
Livermore, California 94550

E-Mail:

8. PERFORMING ORGANIZATION REPORT NUMBER

9. SPONSORING / MONITORING AGENCY NAME(S) AND ADDRESS(ES)

U.S. Army Medical Research and Materiel Command
Fort Detrick, Maryland 21702-5012

10. SPONSORING / MONITORING AGENCY REPORT NUMBER

11. SUPPLEMENTARY NOTES
Report contains color

12a. DISTRIBUTION / AVAILABILITY STATEMENT
Approved for Public Release; Distribution Unlimited

12b. DISTRIBUTION CODE

13. ABSTRACT (Maximum 200 Words)

Ultrasonic transmission tomography holds out the hope of being a discriminating tool for breast cancer screening that is safe, comfortable, and inexpensive. From its inception, however, this imaging modality has been plagued by the problem of how to quickly and inexpensively obtain the data necessary for the tomographic reconstruction. The specific aim of this research is to determine how best to adapt a new microfabricated ultrasonic sensor (currently under development for defense applications) into a breast cancer screening tool. The sensor converts an acoustic wavefront into a modulated optical signal over an entire imaging plane. Using this device, it should be possible to obtain the data necessary for 3D imaging of a breast in a short time, without ionizing radiation, and without the need for compression of the breast. The first year focused on refinement of the sensor design and development of reconstruction algorithms. We have improved the sensor speed and robustness. We have implemented two different types of 2D reconstruction algorithms, based on filtered backpropagation and adjoint methods of solution. We have developed acquisition protocols that obviate the need for optical calibration, and have performed an acoustical calibration. We constructed an ultrasound tank with a rotation stage, and we acquired data from a 3D phantom. The modeling simulations of the data and the actual data from the phantom were in good agreement. We have explored techniques of physician-friendly display, and developed an initial approach for data display from patients.

14. SUBJECT TERMS
Breast Cancer, ultrasound, transmission ultrasound, opto-acoustic imaging, early detection

15. NUMBER OF PAGES
26

16. PRICE CODE

17. SECURITY CLASSIFICATION OF REPORT Unclassified	18. SECURITY CLASSIFICATION OF THIS PAGE Unclassified	19. SECURITY CLASSIFICATION OF ABSTRACT Unclassified	20. LIMITATION OF ABSTRACT Unlimited

NSN 7540-01-280-5500

Table of Contents

INTRODUCTION:

Ultrasonic transmission tomography holds out the hope of being a discriminating tool for breast cancer screening that is safe, comfortable, and inexpensive. From its inception, however, this imaging modality has been plagued by the problem of how to quickly and inexpensively obtain the data necessary for the tomographic reconstruction. The specific aim of this research is to determine how best to adapt a new microfabricated ultrasonic sensor (currently under development for defense applications) into a breast cancer screening tool. The sensor converts an acoustic wavefront into a modulated optical signal over an entire imaging plane. Using this device, it should be possible to obtain the data necessary for 3D imaging of a breast in a short time, without ionizing radiation, and without the need for compression of the breast. In the first year the research focused on refinement of the sensor design and development of reconstruction algorithms. In the second year the research focused on enlarging the area of the sensor, improving the reconstruction algorithms, doing phantom studies, and developing physician-friendly display.

Final Report Body:
In this report we detail the two years of development and design of our optically parallel ultrasound sensor (OPUS). The tasks that were addressed in the first year were: sensor refinement, reconstruction algorithm development, and sensor calibration. The second year's tasks were to enlarge the sensor aperture, improve the reconstruction algorithms, use the system to acquire data on a phantom, and investigate physician-friendly display strategies.

BACKGROUND:
Scientific Basis:
The basic physical principle we are using to do ultrasonic sensing is frustrated total internal reflection (a consequence of optical refraction)[1,2]. Refraction occurs when a wave crosses an interface between media in which the speeds of light are different (i.e. of different refractive indices) [Snell's Law]. If light moves from a slow medium to a fast one, there is a critical angle, $\theta_c = \sin^{-1}(n_1/n_2)$ (where n_2 is the index of refraction of the slow medium and n_1 is the index in the fast medium), beyond which the light is totally reflected. This simple picture ignores the evanescent wave, which extends outside the high index medium, falls off exponentially in amplitude to almost zero within one wavelength beyond the interface, and does not propagate. Frustrated total internal reflection occurs when another slow medium intercepts the evanescent wave. Some light tunnels through the gap and propagates into that medium. The amount of light that tunnels is related to the materials involved, the polarization, and the gap width (see Figures 1 and 2).
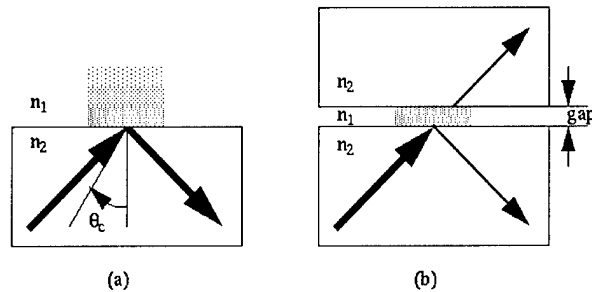

Figure 1. (a) Total internal reflection (TIR) occurring at the interface between an optically slow medium (n2) and a fast medium (n1). The evanescent wave extends into the fast medium. (b) Frustrated total internal reflection occurs when another slow medium intercepts the evanescent wave.
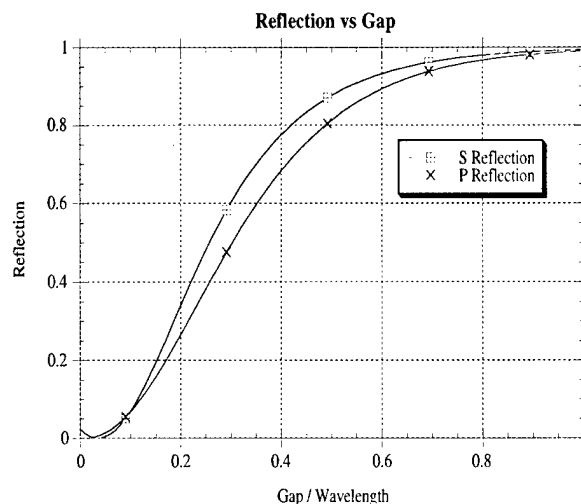

Figure 2. Reflection vs. gap size at the interface between slow and fast media. S and P refer to optical polarization.

Our sensor uses frustrated total internal reflection to make an incident ultrasonic wave modulate a pulsed beam of light, which is then acquired by a camera and computer. A sequence of images, each taken with the optical pulse at a different source acoustic phase, enables us to reconstruct the ultrasonic phase and amplitude over an entire 2-D surface.

Optics:
We exploit frustrated total internal reflection by building an array of acoustic pixels. Each acoustic pixel is composed of a thin (0.1 micron) silicon nitride membrane suspended on short (0.2 micron) gold walls over an optical substrate. The gap between the membrane and the optical substrate is filled with air (figure 3). The membrane is exposed to the ultrasonic couplant. When an ultrasonic pressure wave travels through the couplant and impinges on the acoustic pixel, the membrane deflects, causing a change in the amount of light reflected from the total internal reflection surface of the acoustic pixel. An array of acoustic pixels can be used to modulate a beam of light.
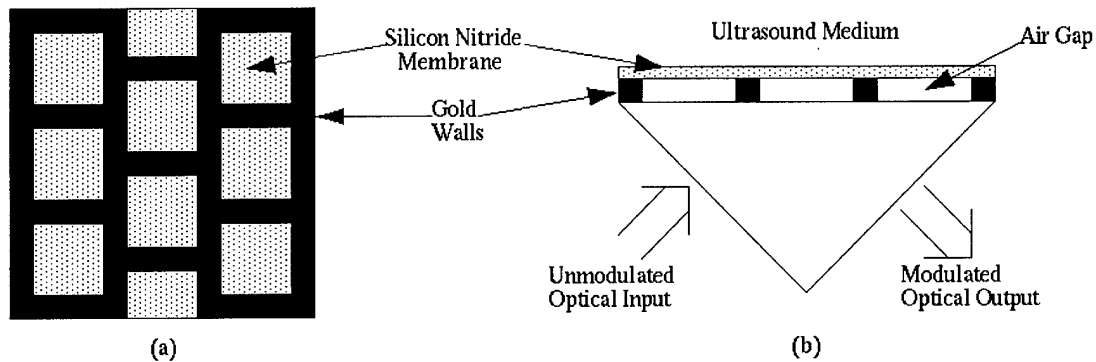
Figure 3. (a) Top view of an array of acoustic pixels. (b) Side view showing acoustic pixels mounted on optical substrate

Just as a strobe light can be used to watch the vibration of a drumhead, we are using a strobed optical source to watch the relative phases and amplitudes of tens of thousands of acoustic pixels, all at once. Given a sequence of images and calibration data, we can extract the relative phase and amplitude of the vibration, and thus extract the relative pressure phase and amplitude at each acoustic pixel. To obtain this information we illuminate the sensor with ten sequences of optical pulses, each sequence timed to act as a strobe light at a specific acoustic phase (figure 4).
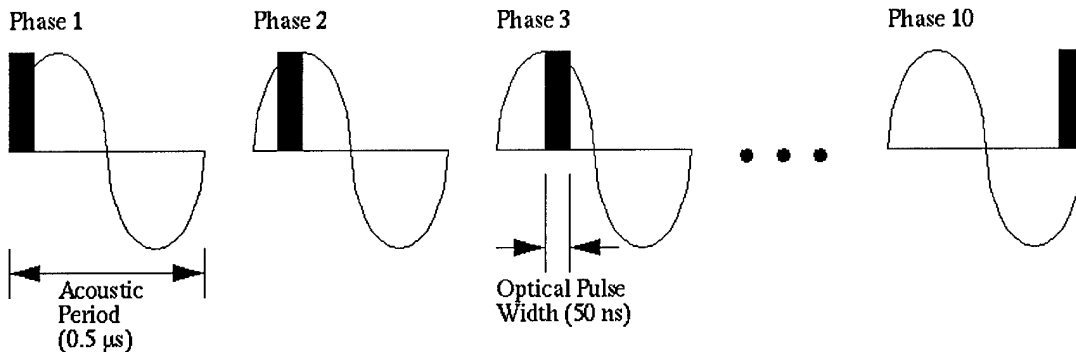
Figure 4. Ten images are taken, each with the optical pulse at a different position in the acoustic period.

We extract the phase and amplitude at each pixel by fitting the intensity at that pixel through the sequence to the form $I = B + A \sin(2 \pi i / 10 + C)$ where I is the intensity, B is the background, A is the amplitude of the sinusoidal variation, i is the index of the image in the sequence, and C is the phase of the variation.

The optical train of this device is as follows: we illuminate the sensor using an LED, the light from which is homogenized, polarized, and collimated. We acquire the reflection using either a CCD still camera or a video camera.

Acoustics:
The imaging technique we are interested in is transmission ultrasound. In this modality, an acoustic source sends out a pressure wave through a couplant, such as water, oil, or medical ultrasound gel, to the object of interest. The pressure waves are transmitted through the object, being modified in amplitude and phase along the way. The pressure wave emerges from the object of interest and travels, via the couplant, to our acoustic sensor.

Our sensor works because the pressure wave flexes the membrane, causing it to vibrate with a phase and amplitude that are functions of that wave. In designing our sensor, we needed to have a membrane with a frequency response high enough to vibrate at the frequencies of interest to us (approximately 2 MHz).

Design Parameters:
There are many material and operational parameters that must be chosen correctly in order to make a working OPUS. Among these are the membrane and wall materials, membrane thickness, wall height, acoustic pixel size, ultrasound operating frequency, optical source characteristics, optical pulse characteristics, and camera characteristics.

Some of these parameters were simple to choose, such as the material for the membrane. The fabrication processes available to us restricted our choice of membrane materials to silicon and silicon nitride. As we wanted to do this work with visible light, we chose to use a silicon nitride membrane.

Other parameters were more difficult to choose, as there was significant interaction between them. For instance, the membrane thickness and the acoustic pixel size interact with each other to effect the sensitivity and frequency response of the sensor. Thus, we relied on modeling to narrow the ranges of these parameters.

Modeling:

We began our work on this project by modeling as many of the systems and processes as possible. We used an in-house reduced-dimension finite-difference time-domain Maxwell's solver (TSARLITE)[8] to model the optical aspects of the sensor (FTIR), a 3-D mechanical dynamics code (DYNA3D)[13] to model the acoustic responses of the membranes and their supports, and a reduced-dimension Beam Propagation Method code (BEEMER)[8] to model the imaging system as a whole.

Using TSARLITE we were able to determine the ranges where we could expect FTIR to be useful, and bounded the permissible thickness of the membrane and the heights of the supports it would stand upon. This modeling was used to optimize the optical aspects of the initial design.

BEEMER (originally a scalar diffraction optics code) was used to examine the issues that arise when the sensor is used for diffraction tomographic imaging. It was used to model the tomographic data acquisition process, as well as a number of reconstruction algorithms.

The simulation program used most heavily was DYNA3D. We used this program to model our initial sensor design, a membrane suspended on an array of posts. DYNA3D showed that this design had neither the sensitivity nor the frequency response necessary to allow us to acquire the data we required. Guided by our simulations, we developed a more responsive design, a set of resonant membranes suspended on walls. Simulation showed this design was responsive and sensitive, but had problems with cross-talk and drift of the resonant frequency as a function of hydrostatic pressure (see Figure 5). Further simulation allowed us to modify the design by offsetting the cells and varying their size so as to greatly reduce cross-talk (see Figure 6).

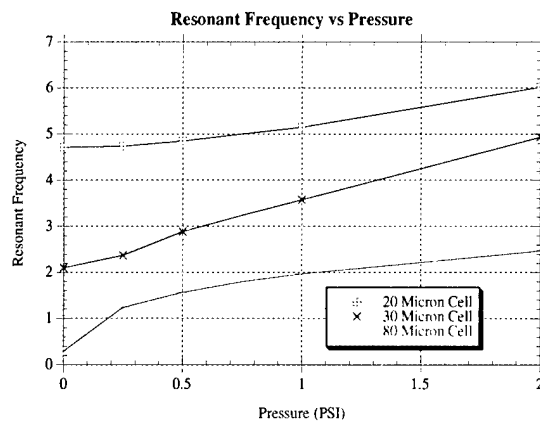**Resonant Frequency vs Pressure**

Figure 5. DYNA3D simulation led to these curves of expected resonant frequency with respect to hydrostatic pressure.
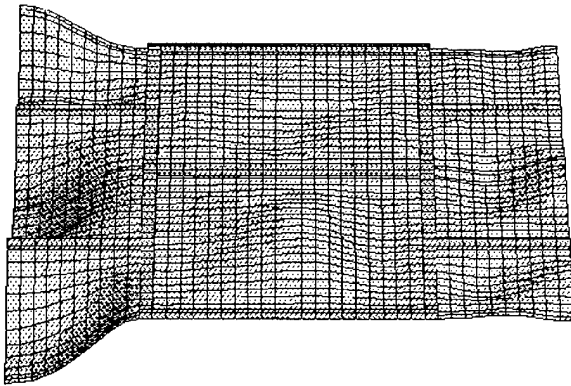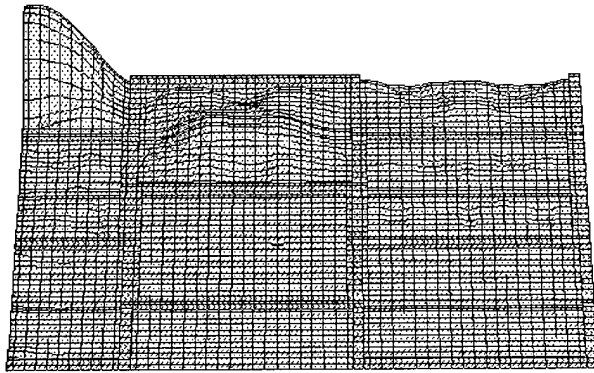

Figure 6a

Figure 6b

Figure 6. Simulation showed crosstalk between acoustic pixels to be a problem. Only the acoustic pixel in the upper left is stimulated. Staggering the acoustic pixels as in (a) reduces the crosstalk, but additionally staggering the resonant frequencies of the acoustic pixels as in (b) reduces the crosstalk significantly.

Simulation led us to a reasonable first design, but we still needed to do experiments to verify the simulations, and get proof of principle results. To do these experiments we built a test system.

Fabrication:
The membrane and its supports are fabricated as depicted in Figure 7.

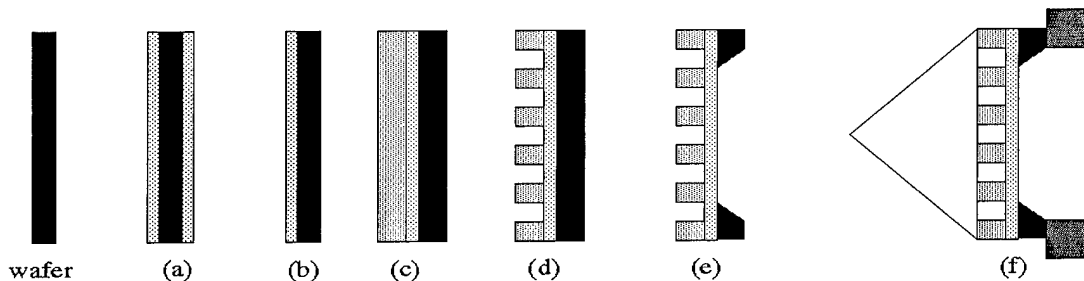

wafer (a) (b) (c) (d) (e) (f)

Figure 7. (a) The silicon wafer has nitride deposited on both sides. (b) The nitride is etched away on one side. (c) A layer of gold is deposited on the nitride. (d) The gold is etched to leave support walls. (e) The silicon is etched from the back, leaving a frame that supports the whole system. (f) The membrane and walls are bonded to the optical substrate , and then mounted to the support plate.

Sensor Parameters:
As a result of proof-of-principle experiments, we had the information necessary for the design and fabrication of the first generation sensor. The acoustic pixel size is 70 microns square, with a 0.1 micron thick membrane, mounted on walls 0.2 microns high. The active aperture is 7 mm square. The sensor is currently being operated at a frequency of 2MHz, at acoustic powers of 20-200 mW/cm^2.

Sensor Noise Characteristics:
The CCD camera we are using is an Apogee Instruments AP1. The images it provides are 760 x 510 pixels, each of which is 16 bits deep. We expose the CCD for one second (two million pulses). We are using a HP 214B pulse generator to send 50 nanosecond 2.8 volt pulses to a red LED.

To determine the purely optical noise characteristics of our data, we collected a set of 40 images with no acoustic excitation. The noise is approximately Gaussian with standard deviations

extending from 24 to 60 counts. In taking data, with the acoustic and optical parameters as above, we collect 90 sequences of images and average them, reducing the noise by a factor of 9. Our data have a sinusoidal variation in amplitude of 30 to 100 counts.

Data Acquisition System:

The data acquisition system consists of an OPUSensor, a tank with an acoustic source and object of interest, and the optics. The system is illustrated in schematic form in figure 8. A Telulex SG-100A arbitrary waveform generator (AWG) provides both a 2 MHz CW signal and an optical pulse synchronization signal. This waveform generator has the ability to generate an arbitrary waveform (which we used to produce a 2 MHz sinewave to send to the amplifier) and an arbitrary sync pulse (which we used to drive the optical pulse generator) simultaneously, under computer control. The 2 MHz sinusoid is amplified and fed through the power meter to the acoustic source in the water tank. The sync signal goes to the pulse generator, which in turn excites the optical source as a strobe light. The pulse generator output and the oscillator output are both fed to an oscilloscope to allow the user to place the optical pulse at any point in the acoustic phase, although this is usually under computer control. The optical pulses are homogenized, polarized, collimated, and fed through the prism to the sensing surface, and the reflected light is captured by the camera and saved in the computer. The user has control over the oscillator frequency, the amplifier gain, the camera exposure time, the optical pulse width, amplitude, and placement in the acoustic phase, as well as the depth of the water in the tank.

During a typical experimental run the water tank was filled to the desired depth, and the acoustic power level, camera exposure time, optical pulse width, and optical pulse amplitude were set. The object of interest was positioned between the acoustic source and the sensor. Sequences of ten images were acquired, each with the optical pulse occurring at a different acoustic phase. Both object data and calibration data (without the target) were acquired.
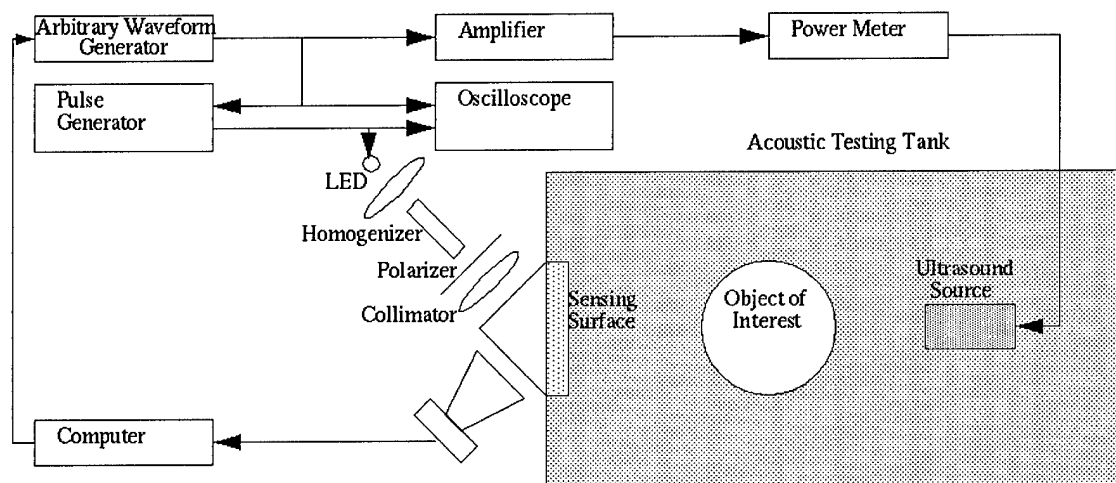

Figure 8. Schematic view of the data acquisition system. The arbitrary waveform generator output is sent to the amplifier (to provide the acoustic signal to the transducer) and the pulse generator (to provide the optical signal). The optical pulse is homogenized, polarized, collimated and sent to the sensing surface. Upon reflection it is acquired by the computer controlled camera. The object of interest is optional.

TASKS:

Task 1: Sensor Refinement.

The refinement of the sensors was a continuous process over the two years of the grant. Sensor refinement entailed optimizing sensitivity, improving manufacturing techniques, and increasing the speed of data acquisition.

Over the two years, we experimented with modifications to the sensor membrane to improve the sensitivity. We found experimentally that the resonances of the acoustic pixels are very broad; therefore, there was little to be gained by adjusting their area for acoustic optimality. Instead we increased the acoustic pixel size slightly so as to increase the area for optical illumination and improve our optical signal to noise ratio.

MEMS Changes:

We have made multiple design changes to the sensor:

1. We changed the way that the sensor and prism are assembled. Previously, sensors were assembled by taking a porthole, laying the sensor on top, then gluing a prism over the top (see Figure 9). This turned out to be a suboptimal assembly technique, often leading to leaks around the membrane frame and destroyed sensors. Now, we glue the membrane frame to the plate and then press the prism against the membrane, supporting the prism from the rear with a frame attached to the plate (see Figure 10). This insures that the membrane frame will not leak, and it allows easier pre-installation testing of the membranes for water-tightness.

Glue-line

Glue-line

Prism viewed parallel to its hypotenuse

Porthole Plate cutaway
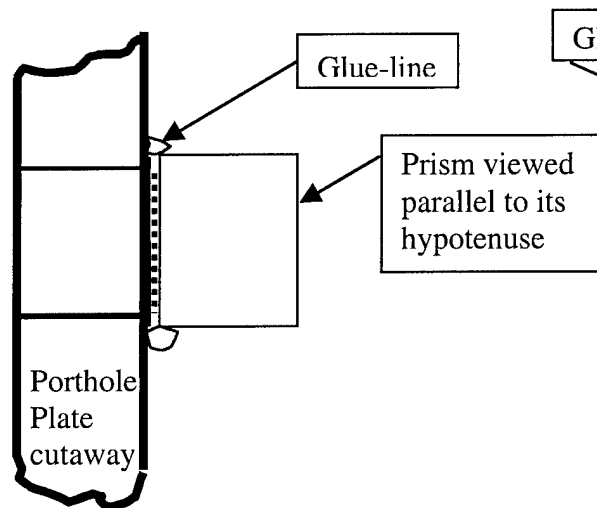
Frame supporting prism, bolted to the plate

Figure 9
Initial prism/sensor assembly.
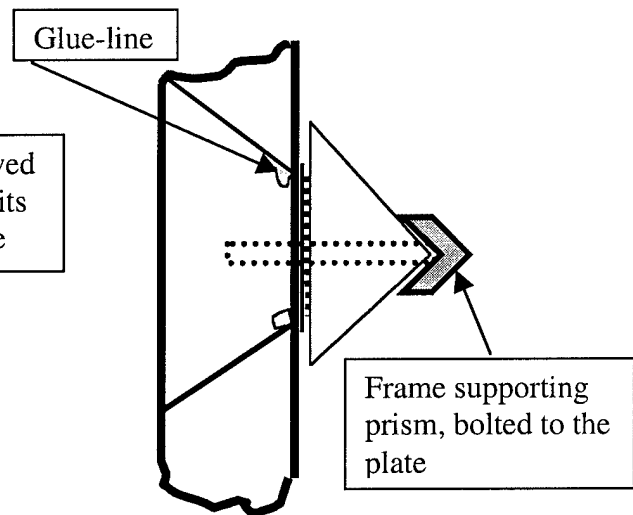The prism was glued over the sensor membrane.

Figure 10
Current prism/sensor assembly. The sensor is glued to the plate, then the prism is pressed against it by a framework. The hole in the plate has been chamfered to increase the acoustic access to the sensor.

- We increased the robustness of the membrane. Originally, our membranes were fabricated under high tension (500MPa). By altering the fabrication parameters, lower tension (100MPa) membranes were produced. Prior to this change, membranes would rupture at the slightest provocation. With the lower tension membranes, the membranes in the 0.7 cm frames last indefinitely (no failures since the change).

- The sensor membrane size was adjusted from 1cm on a side to 0.7 cm on a side. Although this reduced the aperture size, it improved the sensor fabrication yield and robustness.

- We began the process of scaling up the sensor aperture by using paned windows of the .7 x .7 cm membranes. We designed and fabricated membranes consisting of a 5 x 3 paned array, with at least a 90% active area. However, we had persistent difficulty with the larger paned arrays. The silicon wafers available to the MEM and the electronic industry are not available optically flat. Over a 4 cm. wide silicon wafer, the surface could be bowed at least 1micron. This does not seem like a large amount of distortion, but relative to the 0.2 micron high walls of the sensor, it is a large deformity. The resultant large area membranes could not be assembled into sensors because they developed leaks when applied to the optically flat prisms and subjected to hydrostatic pressure.
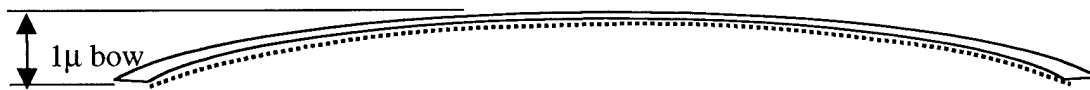

Figure 11 Larger area sensors were difficult to manufacture because of unavailabliity of flat silicon wafers.

- Because of the persistent problem with the larger area sensors, we developed a completely new concept for the ultrasound to optical transducer. Since the basis of the OPUS design is small closed air cells adjacent to a prism, we deduced that a plate coated with a transparent film with bubbles should be able to function in the same capacity as the OPUS membranes. The bubble-plate that we developed consisted of the sensor prism coated with a hydrophobic material in which small holes had been made (see Figure 12). The idea is that each of these holes traps and retains a bubble. The bubble retains its integrity because of the surface tension of the water, not because of a membrane, so it should be more sensitive to the ultrasonic excitation, as well as having a higher frequency response. We spent considerable effort trying to engineer this concept, and built several prototypes. However, we had a persistent problem keeping the air bubbles in the film. Our first attempts involved standard photoresists and lithography. However, since the aspect ratio (depth/width) of the holes must be high enough to trap a bubble, and a coating thickness of <0.2 microns was necessary, it proved impossible to get small enough diameter holes by this process. Next, we used a LLNL proprietary process to make 0.2 micron diameter holes in a Lexan coating, but the resultant plate was still unable to maintain air bubbles.
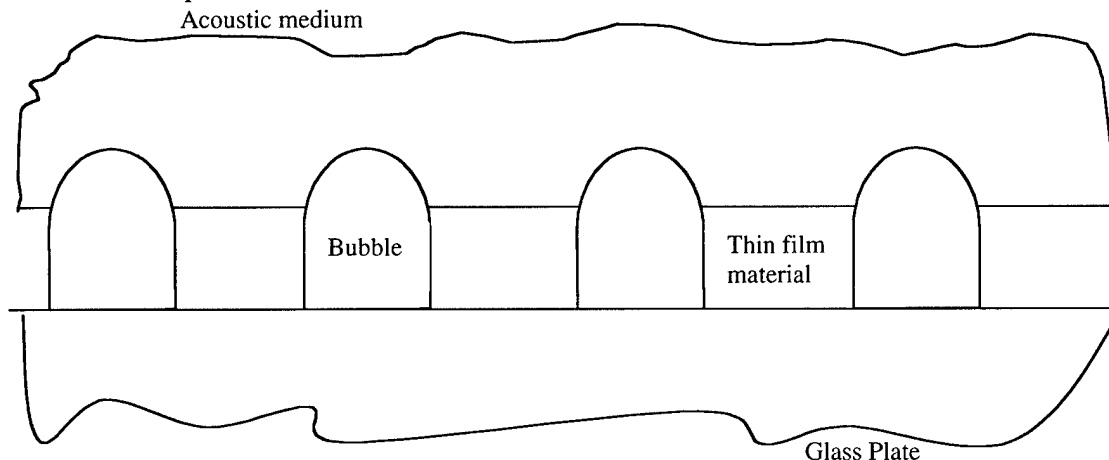

Figure 12. Bubble-plate concept for enlarging the sensor.

Optical Changes

By changing from our Apogee digital camera to a video camera, we have reduced acquisition times by a factor of approximately 100. The Apogee camera required 1 second to acquire a frame of data and 8 seconds to offload it into the computer. We are able to acquire video images at a rate of 10 frames per second. This has significantly changed the way we acquire data. Previously, we set the optical pulse at a specific acoustic phase for each image acquired. This added additional time to each frame acquired, but spread long-term drifts in the data acquisition system parameters over all phases. This was important because it could take 3 hours to collect a sequence of data. Now we can set the optical pulse in the acoustic phase and acquire all the frames we wish to average in less than 10 seconds. Unfortunately, the video camera we used in the first year was noisier than the Apogee camera. However, by acquiring more frames we reduced the noise. Ultimately, we purchased a high-speed video camera with excellent signal to noise ratio. Now images are acquired at an even faster rate, and the fast camera enables signal averaging with minimal time expenditure.

In switching to a video camera we have qualitatively changed the way the sensor can be used. We have found that at video speeds the eye's filtering ability enables one to see changes in the pressure wavefronts impinging on the sensor in real time. By changing the timing of the optical pulse, one can infer the shape of the wavefront.

Task 2: Reconstruction Algorithm Development.

As a crucial step in verification of any reconstruction algorithm, a simulator had to be developed that could model both the propagation of sound through a phantom and reconstruction of images using the data. We built the simulator, based on the BEEMER scalar paraxial wave propagation code. This allowed us to import simulated phantoms, model the propagation of sound through them, and experiment with reconstruction algorithms. We used a linear Rytov-approximation based, filtered backpropagation algorithm[3] to do the 2D reconstruction experiments in the first year, and a nonlinear adjoint method algorithm in the second year.

The two most commonly used simplifications in linear diffraction tomography are the Born and Rytov approximations. The Born approximation assumes that there are no large differences in the index of refraction anywhere in the problem space[4,5]. The Rytov approximation assumes that there are no large gradients in the index of refraction[6]. Both assume that there is no multiple scattering. Devaney first published the filtered backpropagation algorithm in 1982[3]. Filtered backpropagation uses a more general form of the Fourier projection-slice theorem, and reduces to filtered backprojection in the zero wavelength limit. Whereas the Fourier transform of a zero wavelength projection in real space equals a radial slice of Fourier space perpendicular to the angle of the projection, the Fourier transform of a finite wavelength projection is equal to a semicircle in Fourier space which grazes the origin at an angle perpendicular to the angle of the projection (see figure 13). In the zero wavelength limit, filtered backprojection is a fast and simple way to reconstruct images from projections[7]. In the case of finite wavelength, filtered backpropagation is an attractive reconstruction method. With filtered backprojection, the projection is filtered and then distributed into the reconstruction space to generate an image. Filtered backpropagation requires that the filtered projection be propagated across the reconstruction space. Propagation is a more computationally intense operation than simple projection.

Based on the experiments we performed with the simulator, we built a stand-alone 2D reconstruction code which used a simple implementation of the Devaney Rytov filtered backpropagation

Normal Space

Fourier Space

wave
vector

Plane
Wave
Insonification

Planar
Sensor

Obj

(a)

Normal Space

Fourier Space

wave
vector

Plane
Wave
Insonification

Planar
Sensor

Obj

All wave
vectors
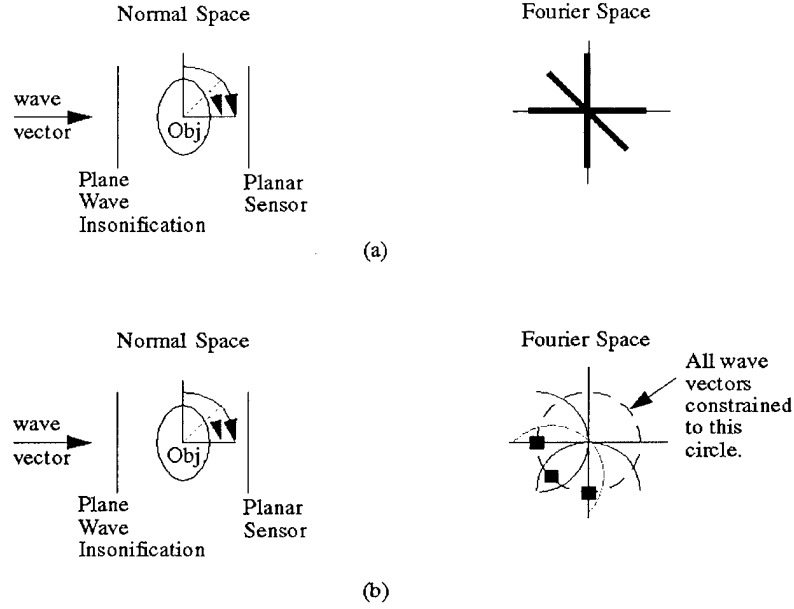constrained
to this
circle.

(b)

Figure 13. The difference between zero and finite wavelength projections: a) zero wavelength limit, Fourier transforms of projections become radial lines, b) finite wavelengths, Fourier transforms of projections become semicircles.

During the second year of the project, we investigated the adjoint method of nonlinear iterative reconstruction[9,10]. In a nonlinear reconstruction algorithm, a calculation is made of what data would have resulted from the current reconstruction (forward model). The output of the forward model is compared to the actual experimental data, and the difference is used to generate an update to the reconstruction. A one dimensional optimization is performed to determine how much of the update to apply. This involves many iterations of the forward model (which is why it is crucial to have a fast model). This process is repeated until the modeled data match the experimental data. The adjoint method is a fast and efficient way to generate the update to the distribution of the index of refraction we wish to determine.

To simplify the data processing we assumed that there was insignificant multiple scattering and that large deviations (>10%) in sound speed do not occur[14]. This allows us to use a paraxial wave equation solver for doing the forward modeling. A more correct forward model would be a Helmholtz equation solver, but this would be a much larger computational burden. As there are no published derivations for the paraxial adjoint method, we have included the derivation in Appendix I. The final result of the derivation is that the current update to the index should be a multiple of the imaginary part of $\psi(r)\psi^-(r)n(r)$, where $\psi(r)$ is the field computed with the current reconstruction, $\psi^-(r)$ is a backpropagation throught the current reconstruction with the error field $\psi(r_{obs}) - \psi_{exp}(r_{obs})$, and n(r) is the current reconstruction.

Compared to the linear reconstruction methods, the adjoint method yielded far more accurate reconstructions with our data, although at a much higher (by a factor of ~60) computational cost. However, computational costs becomes less and less important as computer speed increases, so the accuracy of the reconstruction is far more critical than the speed of the calculation.

Task 3: Sensor Calibration.

Because we have developed experimental protocols that include normalizing the subject data to calibration images, optical calibration is unnecessary. Thus, even though the illumination is not uniform over the whole sensor, the calibration images normalize out the nonuniformities.

We have determined that the acoustic response of the sensor is linear. We acquired data using 10 different input voltage levels (0.0V peak to peak to 9.0V peak to peak to the amplifier) (see figure 8). We collected sequences of data for each of these levels and extracted from them the amplitudes at each acoustic pixel. The amplitude vs. power level at each pixel is linear, with correlation coefficient of 0.984. The highly linear nature of the data indicates that the deflections of the membrane are very small because (as can be seen in figure 2) a large deflection would have excited the sensor into the nonlinear portion of the optical response curve.

By measuring the power input to the source transducer, we have determined the minimum pressure required to optically observe deflection of the membrane. The membrane can detect pressure changes of 7kPa (actually, considering the efficiency and location of the source transducer, it is likely seeing at least a factor of 10 smaller pressure).

Task 4: Phantom Tank Studies.
Diffraction Tomography Experiments:

For a test of diffraction tomography using the sensor we built a phantom with a constant 2D cross section. The phantom consisted of three pieces of 0.5mm diameter fishing line placed at 120 degree separations around a 1.5 mm radius circle (see figure 14). These materials and configuration were selected because the plastic has an acoustic index not too different from the liquid medium (a situation that mimics the variability in acoustic index in the breast), and the sizes are comparable to what we plan to image with the system. We used water as our acoustic medium; therefore, an acoustic frequency of 2 MHz had a wavelength of 0.74 mm. Using our simulator (a modification of the BEEMER modeling code[8]) we determined that it would be possible to do a diffraction tomographic reconstruction with 18 projections.
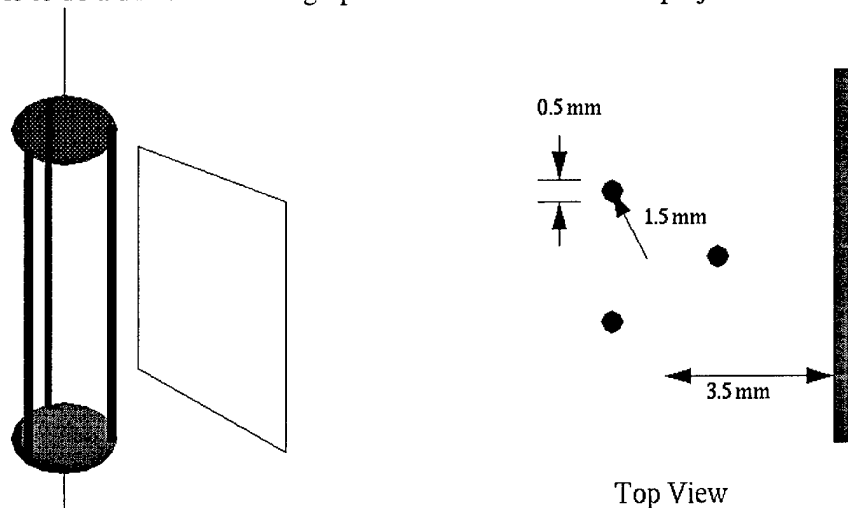

Figure 14. The relationship and dimensions of the phantom and the sensor

We utilized a constant cross-section phantom so that 2D reconstruction (rather than 3D) could be performed. The full 3D reconstruction algorithms are still under development.

Equipment Modifications:
We mounted a rotation stage above the tank and suspended the phantom 3.5 mm in front of the sensor. The rotation stage was manually controlled. We mounted the source transducer far enough away (10 cm) to illuminate the phantom with a planar 2MHz ultrasound wave.

Data Acquisition:
The data necessary for reconstruction of the phantom are a set of 18 projections, where each projection consists of the relative acoustic phase and amplitude over the entire sensor surface. The acoustic period was divided into ten discrete phases, as sufficient to extract the sinusoidal parameters at each acoustic pixel. A set of 10 images is a sequence from which phase and amplitude can be extracted. We took 90 sequences that were then summed, to increase the signal to noise ratio.

The data for each projection (18 projections overall) were acquired under computer control. The data consisted of 90 sequences of 10 images (one image with the optical pulse at each of 10 acoustic phases). To acquire each image, the sinusoidal waveform was downloaded into the arbitrary waveform generator with the sync pulse at the appropriate acoustic phase, the camera shutter was opened for 1 second, then the data was downloaded to the computer. The image was summed into a composite image for the appropriate phase. Upon completion of the acquisition of the 90 sequences, the final summed images were saved to disk. After each projection was acquired, the phantom was rotated 20 degrees, and acquisition was repeated.

After the projection data were acquired, we obtained calibration data by removing the phantom and averaging 90 sequences of 10 phase images.

Data Reduction:
After data collection we had 18 projection sequences and one calibration sequence, each consisting of 10 summed images. For each pixel in every sequence, the intensity was fit to a sinusoid with phase plus a background. Since the illumination over the optical field was not uniform (intentionally, to minimize costs), the sinusoidal amplitude was normalized by the background intensity. For every pixel in each sequence we recorded the amplitude ratio and the phase. To extract relative pressure amplitude, we normalize the image of the projection ratios by the image of the calibration ratios, on a pixel by pixel basis. This yielded 18 images of relative pressure amplitude (see figure 15). By subtracting the calibration phase from the target phases, we obtained 18 images of relative phase.
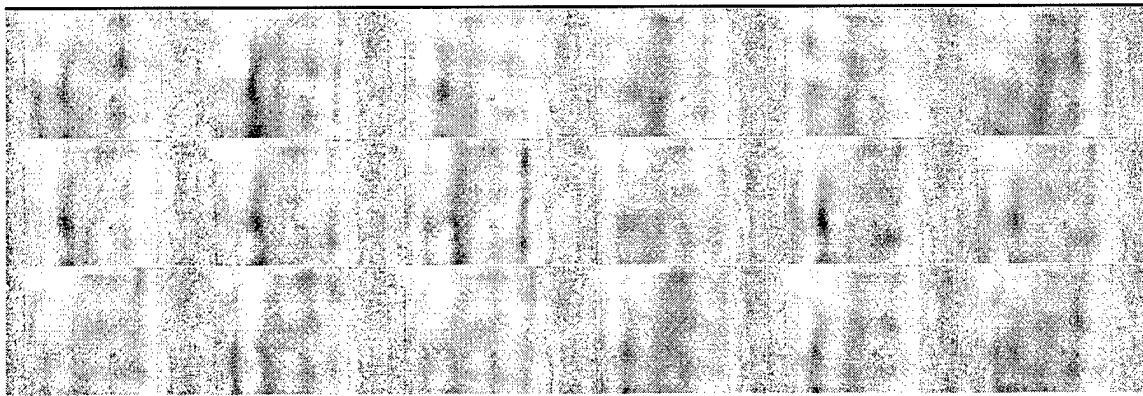

Figure 15. The 18 images of relative pressure amplitude obtained by the OPUS system from the 3-monofilament phantom.

Image Reconstruction:

Using a simple implementation of the Devaney Rytov filtered backpropagation (see task 2 above), we were able to obtain images of both the distributions of sound speed and absorption (see figure 16).
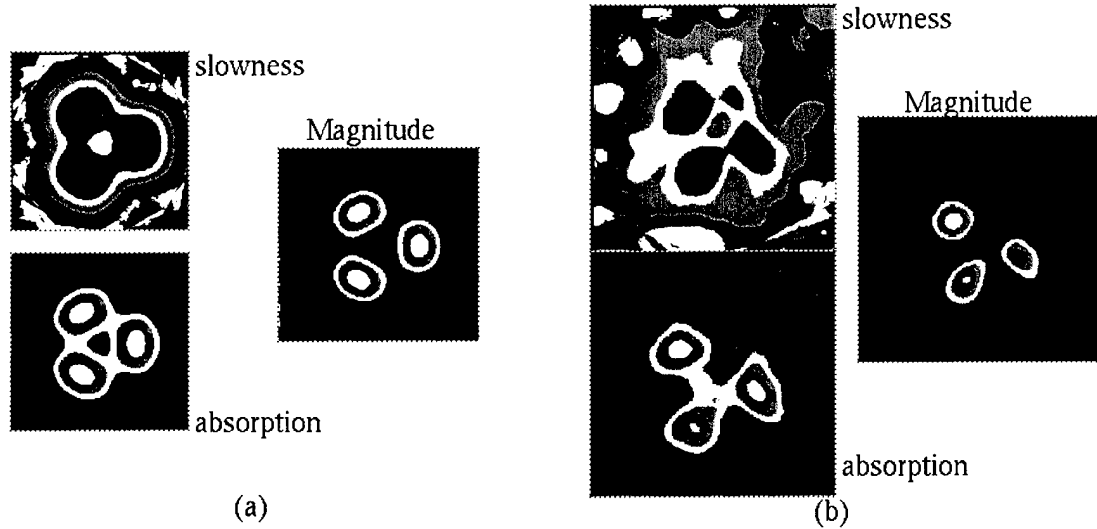

Figure 16. a) Reconstruction of a simulation of the 3-monofilament phantom using Devaney-Rytov filtered backpropagation. b) Reconstruction from the data in figure 14.

In addition to diffraction tomography, we have implemented an adjoint method for the reconstruction of diffraction data[9,10], as seen in Figure 17. This code was used with a paraxial model, but could be implemented with a full Helmholtz model, as well.

Figure17 Reconstruction of a simulation of the 3-monofilament phantom using the Adjoint Method is shown in (a). Shown is the slowness. Compare the improved fidelity of the reconstruction relative to the Devaney-Rytov Method shown in Figure 16a slowness. In (b) are the absorption and the slowness reconstructed from the data in figure 14.
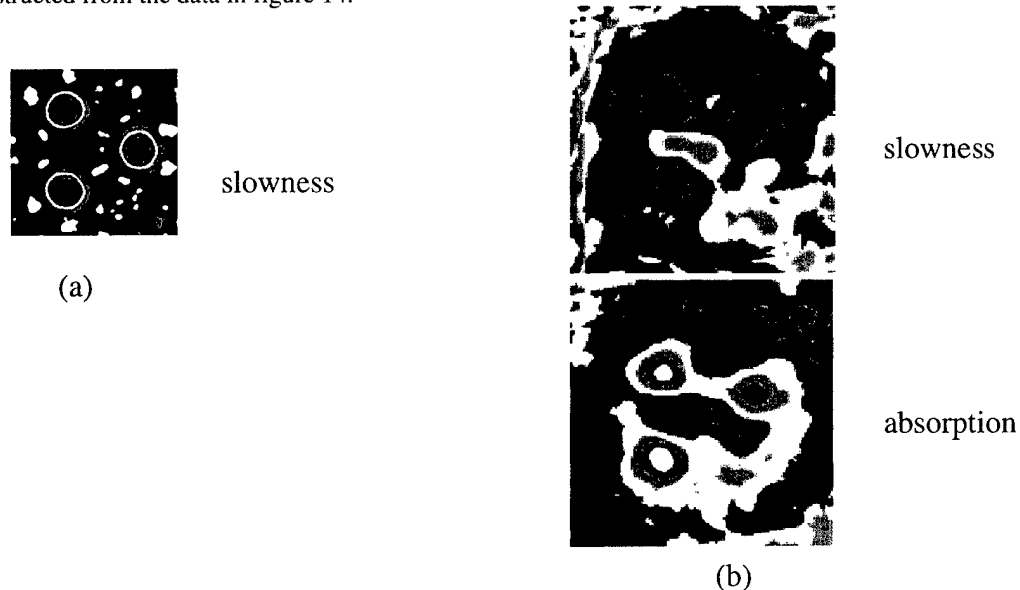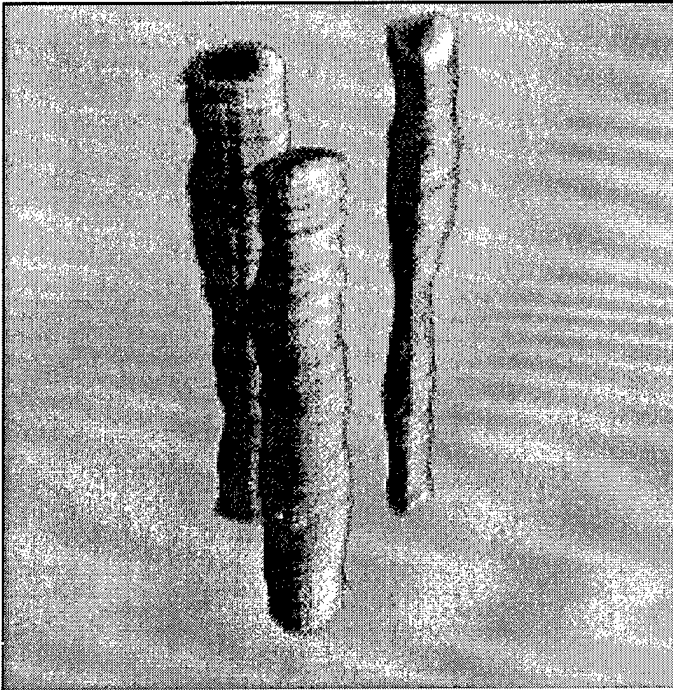
Figure 18. 3 Dimensional rendering of the reconstructed OPUS-imaged phantom sketched in Figure 13. The phantom is three sections of monofilament line, each 0.5 mm in diameter. This reconstruction was accomplished with the Devaney Rytov filtered backpropagation method.

Task 5: Physician-friendly Display
There are several important issues and principles involved in display of breast ultrasound data for visual analysis.

The information must be viewed on both the macro and the micro level for detection of abnormal areas. To that end, the data need to be viewed first in a non-obtrusive grid for orientation, in a position similar to what would be seen in a standing person. A faint line will indicate the skin surface and the deepest scanning margin (See Figure 19) Grey will be used for the background grid and for the deep margin lines, so as to give orientation without distracting from the overlying data (See Figure 20). Black outlines are to be avoided, as they draw the eye to the unimportant delineators, rather than to the displayed data[12].

The colors for sound speed and attenuation will be in yellows and blues, so as to be both visually comfortable and to maximize visual contrast for persons with red/green color blindness. The colors will be translucent to enable visualization of data through the entire breast at once (See Figure 21). Varying color saturation will indicate the scale. It may be desirable to filter values for sound speed and attenuation to display value ranges of greatest interest, avoiding overly dense display. However, it will be necessary to acquire data on an entire breast before it is possible to determine details of optimal display.

After initial survey of the breast, the data can be rotated about all axes or sliced in arbitrary planes to facilitate viewing. Specific volumes can be extracted for viewing without the surrounding tissue.
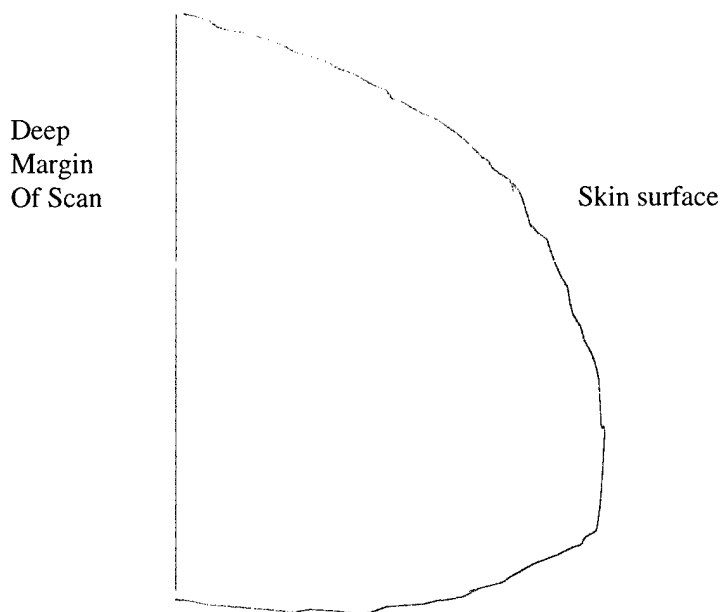
Deep
Margin
Of Scan

Skin surface

Figure 19. Representation of display technique for sound speed, shown in yellow, with color saturation indicating the scale. The skin surface and deepest margin are outlined in grey. This is a lateral view.
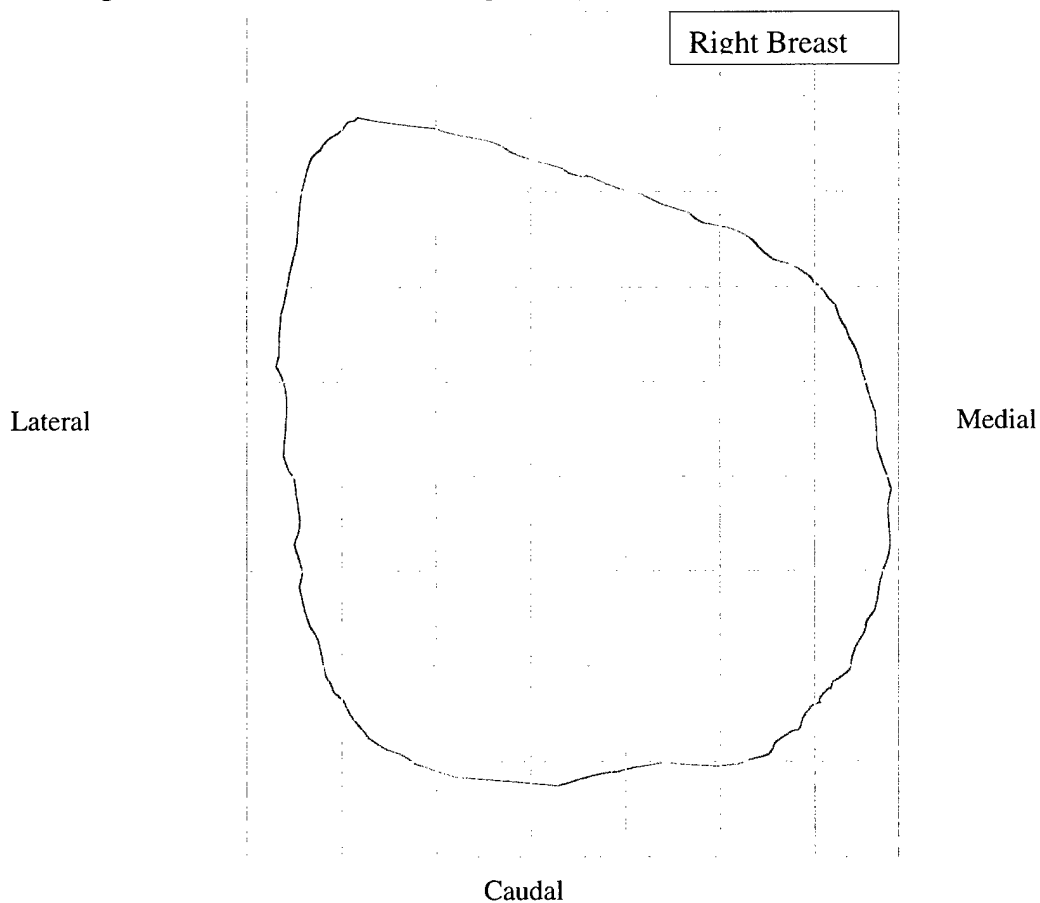
Right Breast

Lateral

Medial

Caudal

Figure 20. Antero-posterior representation of display technique for sound speed, shown in yellow, with color saturation indicating the scale. The deepest margin is outlined in grey. Note that the grid scale is in an even lighter grey than the depth outline, so as to give reference but not intrude on the data.

Rostral

Right Breast

Lateral   Medial
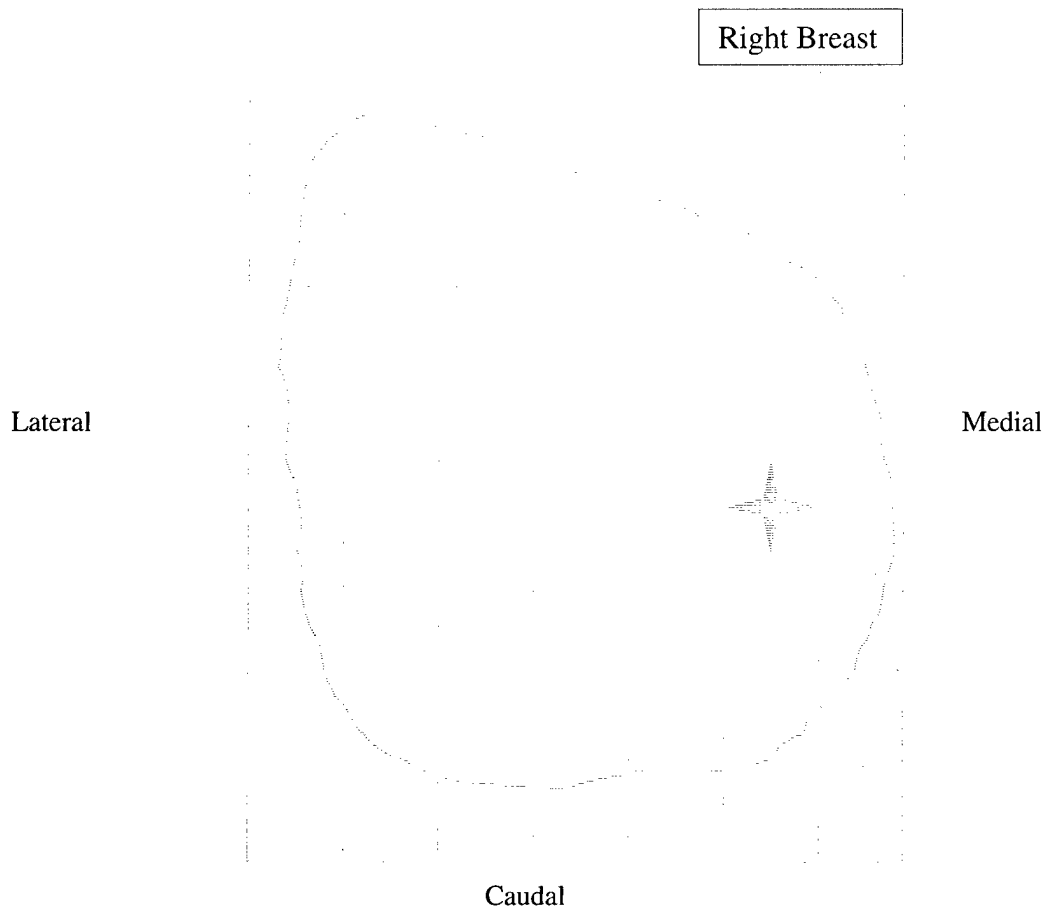
Caudal

Figure 21. Antero-posterior representation of display technique for sound speed, shown in yellow, with color saturation indicating the scale. Attenuation is indicated in blue, with saturation indicating the scale. The deepest margin is outlined in grey

SUMMARY:

We have developed a new type of ultrasound sensor that makes it possible to sense the pressure field over a plane. The sensor uses the phenomenon of frustrated total internal reflection to modulate the reflection of an optical beam depending on the deflection of a 0.1 micron thick silicon nitride membrane that covers an acoustic pixel. Our acoustic pixels are defined by gold walls 0.2 microns tall and enclosing a square air space approximately 70 microns on a side. We have used an array of 10,000 acoustic pixels to acquire data yielding diffraction tomographic images of a 3-monofilament phantom.

We have improved the sensor speed and robustness. We have implemented two different types of 2D reconstruction algorithms, based on filtered backpropagation and adjoint methods of solution. We have developed acquisition protocols that obviate the need for optical calibration, and have performed an acoustical calibration. We constructed an ultrasound tank with a rotation stage, and we acquired data from a 3D phantom. The modeling simulations of the data and the actual data from the phantom were in good agreement.

We have explored techniques of physician-friendly display, and developed an initial approach for data display from patients.

ACKNOWLEDGEMENTS:

KEY RESEARCH ACCOMPLISHMENTS:

Sensor Refinement
- We changed the fabrication process to generate low-tension membranes in 0.7 cm square-frames. These proved far more durable than high-tension membranes in 1.0 cm square-frames.
- We determined that an acoustic pixel size of 70 microns is appropriate for excitation frequencies of up to 2 MHz.
- We incorporated a video-rate camera for data acquisition. It not only increased the speed of acquisition by a factor of 100 but also made the system more like a fluoroscope in that one could watch changes in the acoustic pressure waveform in real-time.

Reconstruction Algorithm Development
- We discovered that our sensor can collect data with a high enough signal to noise ratio that they can be reconstructed into an image.
- We determined that the Rytoff approximation is sufficient for reconstructing our phantom data.
- We developed filtered backpropagation and paraxial adjoint reconstruction codes.

Sensor Calibration:
- We implemented data acquisition protocols such that no prior optical calibration is necessary because optical calibration data are acquired as a part of normal data acquisition.
- We determined that the sensor is linear in its response to acoustic excitation.
- We demonstrated that the sensor can detect pressure amplitudes below 7 kPa.

Phantom Tank Studies
- We modified the test tank to be used for phantom studies.
- We acquired data from a simple phantom.
- We reconstructed images using linear diffraction tomography and adjoint methods of solution.

Physician-friendly Display
- We researched the graphics literature and adopted accepted techniques for optimal data display.

REPORTABLE OUTCOMES:

We have submitted a manuscript to Journal of the Acoustical Society of America for publication.

CONCLUSIONS:

We have developed a new type of ultrasound sensor that makes it possible to sense the pressure field over a plane. The sensor uses the phenomenon of frustrated total internal reflection to modulate the reflection of an optical beam depending on the deflection of a 0.1 micron thick silicon nitride membrane that covers an acoustic pixel. Our acoustic pixels are defined by gold walls 0.2 microns tall and enclosing a square air space approximately 70 microns on a side. We have used an array of 10,000 acoustic pixels to acquire data yielding diffraction tomographic images of a 3-monofilament phantom.

We have improved the sensor speed and robustness. We have implemented 2D reconstruction algorithms. We have developed acquisition protocols that obviate the need for optical calibration,

and have performed an acoustical calibration. We built a phantom tank with rotation stage and imaged a phantom.

The development of this technology is important for the early detection of breast cancer. It offers a potential way of implementing volumetric imaging of the breast without the ionizing radiation and discomfort of x-ray mammography or the cost of MRI. To fulfill this promise, we must scale up the sensor and develop further 3D reconstruction algorithms.

REFERENCES:

1. J. Strong, *Concepts of Classical Optics*, W. H. Freeman and Company, 1958.
2. P. Yeh, *Optical Waves in Layered Media*, John Wiley and Sons, New York, 1988.
3. A. J. Devaney, "A filtered backpropagation algorithm for diffraction tomography," *Ultrasonic Imaging*, **4**, pp. 336-350, 1982.
4. E. Wolf, "Three-Dimensional Structure Determination ofSemi-Transparent Objects From Holographic Data," *Optics Communications*, **1**, pp. 153-156, 1969.
5. R. Dandliker and K. Weiss, " Reconstruction of the Three-Dimensional Refractive Index From Scattered Waves," *Optics Communications*, **1**, pp. 323-328, 1970.
6. A. J. Devaney, "Inverse-scattering theory within the Rytov approximation," *Optics Letters,* **6**, pp. 374- 376, 1981.
7. A. Makovski, *Medical Imaging Systems*, Prentice-Hall, Inc., pp. 125-126, 1983.
8. R. J. Hawkins, J. S. Kallman, R. W. Ziolkowski, "Computational Integrated Photonics," *Engineering Research Development and Technology*, R. T. Langland, C. Minichino, UCRL 53868-92, pp 1.7-1.11, Lawrence Livermore National Laboratory, Livermore, 1993.
9. O. Dorn, H. Bertete-Aguirre, J. G. Berryman, G. C. Papanicolaou, "A nonlinear inversion method for 3D electromagnetic imaging using adjoint fields," Inverse Problems **15**, pp. 1523-1558, 1999.
10. S. J. Norton, "Iterative inverse scattering algorithms: Methods of computing Frechet derivatives," *J. Acoust. Soc. Am.* **106** (5), 1999.
11. F. Natterer, F. Wubbeling, "A propagation-backpropagation method for ultrasound tomography," *Inverse Problems*, **11**, pp. 1225-1232, 1995.
12. E. R. Tufte, *Envisioning Information*, Graphics Press, 1990.
13. R. G. Whirley, B. E. Engelmann, "DYNA3D A Nonlinear, Explicit, Three-Dimensional Finite Element Code For Solid and Structural Mechanics-User Manual", UCRL-MA-107254, 1993.
14. J.F. Greenleaf and R. C. Bahn, "Clinical Imaging with Transmissive Ultrasonic Computerized Tomography," *IEEE Trans. on Biomedical Engineering*, BME-28, pp. 177-185, 1981.

APPENDIX
Paraxial Adjoint Method Fréchet Derivative Derivation
(following the method of Norton[10])

The paraxial wave equation arises from the wave equation:

$$\nabla^2 \Psi - \frac{n^2}{c^2}\frac{\partial^2 \Psi}{\partial t^2} = 0$$

where Ψ is the velocity potential, c is the nominal speed of sound, and n is the acoustic index of refraction. If we assume the following form for Ψ :

$$\Psi(x,y,z,t) = \psi(x,y,z)e^{-i(\omega t - kz)}$$

(where ω is the frequency of interest, and k is the wave number in the z direction) the wave equation reduces to the Helmholtz equation

$$\nabla^2 \Psi + \frac{\omega^2 n^2}{c^2}\Psi \;=\; \nabla^2 \Psi + k_0^2 n^2 \Psi \;=\; \frac{\partial^2 \Psi}{\partial z^2} + \nabla_\perp^2 \Psi + k_0^2 n^2 \Psi$$

where $k_0 = w^2/c^2$, and $\nabla_\perp^2$ is the part of the Laplacian perpendicular to z. Note that up until now we have been dealing with the velocity potential. The perterbation in

the pressure p due to the velocity potential is given by $p = \rho\dfrac{\partial \Psi}{\partial t}$, where ρ is

the density of the acoustic medium. However, given the form of Ψ , we can take the derivative of the Helmholtz equation with respect to time, multiply by $i\rho/\omega$, and then Ψ will be isomorphic with p .

Looking more closely at the partial derivative with respect to z we find

$$\frac{\partial^2 \Psi}{\partial z^2} = [\frac{\partial^2 \psi}{\partial z^2} + 2ik\frac{\partial \psi}{\partial z} - k^2 \psi]e^{-i(\omega t - kz)} \quad .$$

If we assume the first term on the right hand side is insignificant compared to the other two, insert the other two terms into the wave equation, and divide through by the exponential term and $2ik$, we obtain the paraxial wave equation:

$$\frac{\partial \psi}{\partial z} - \frac{i}{2k}\nabla_\perp^2 \psi + \frac{i}{2k}(k^2 - k_0^2 n^2)\psi = 0 \tag{1}$$

We want to find the index distribution $n(\vec{r})$ that most closely matches that which produced the phase and amplitude at the observation points of the problem. This distribution will minimize the weighted squared error functional:

$$E[n(\vec{r})] = \frac{1}{2}\sum_{m=1}^{M} w_m |\psi(\vec{r}_m) - \psi_{obs}(\vec{r}_m)|^2 \tag{2}$$

where M is the number of observation points, w_m is the weight of the mth point, ψ is the solution to the paraxial wave equation with the current estimate of the index distribution, and the ψ_{obs} are the scattering data.

We want to find the $n(\vec{r})$ that minimizes the error. Represent the variation of the error with a change in index distribution this way:

$$\delta E[n(\vec{r})] = \iiint\limits_{space} \nabla_F E(\vec{r}) \delta n(\vec{r}) d^3 r \qquad (3)$$

where δ is the variation operator, and $\nabla_F E$ is the Fréchet derivative (the quantity we are after). Consider what taking the variation with respect to n does to equations 1 and 2:

$$\frac{\partial \delta \psi(\vec{r})}{\partial z} - \frac{i}{2k} \nabla_\perp^2 \delta \psi(\vec{r}) + \frac{ik}{2} \delta \psi(\vec{r}) - \frac{ik_0^2 n^2}{2k} \delta \psi(\vec{r}) - \frac{ik_0^2}{k} \psi(\vec{r}) n(\vec{r}) \delta n(\vec{r}) = 0 \quad (4)$$

$$\delta E[n(\vec{r})] = \Re \sum_{m=1}^{M} w_m (\psi(\vec{r}_m) - \psi_{obs}(\vec{r}_m))^* \delta \psi(\vec{r}_m) \qquad (5)$$

where * is the complex conjugate and $\Re$ means taking the real part.

We define the adjoint field by:

$$-\frac{\partial \tilde{\psi}}{\partial z} - \frac{i}{2k} \nabla_\perp^2 \tilde{\psi} + \frac{i}{2k}(k^2 - k_0^2 n^2) \tilde{\psi} = -\tilde{S}(\vec{r}) \qquad (6)$$

where $\tilde{\psi}(\vec{r})$ is the adjoint field and $\tilde{S}(\vec{r})$ is the adjoint source given by

$$\tilde{S}(\vec{r}) = \sum_{m=1}^{M} w_m (\psi(\vec{r}_m) - \psi_{obs}(\vec{r}_m))^* \delta(\vec{r} - \vec{r}_m) \ . \qquad (7)$$

Note that here $\delta(\vec{r} - \vec{r}_m)$ is the dirac delta function (impulse function).

We can see that (7) is such that we can cast (5) as

$$\delta E[n(\vec{r})] = \Re \iiint\limits_{space} \tilde{S}(\vec{r}) \delta \psi(\vec{r}) d^3 r \ . \qquad (8)$$

If we substitute (6) into (8) we find that

$$\delta E[n(\vec{r})] = -\Re \iiint\limits_{space} [-\frac{\partial \tilde{\psi}}{\partial z} - \frac{i}{2k} \nabla_\perp^2 \tilde{\psi} + \frac{i}{2k}(k^2 - k_0^2 n^2) \tilde{\psi}] \delta \psi \, d^3 r \ . \qquad (9)$$

We use the following identities:

$$\delta \psi \nabla_\perp^2 \tilde{\psi} = \tilde{\psi} \nabla_\perp^2 \delta \psi + \nabla_\perp \cdot (\delta \psi \nabla_\perp \tilde{\psi} - \tilde{\psi} \nabla_\perp \delta \psi) \qquad (10a)$$

and

$$\delta \psi \frac{\partial \tilde{\psi}}{\partial z} = -\tilde{\psi} \frac{\partial \delta \psi}{\partial z} + \frac{\partial}{\partial z}(\delta \psi \tilde{\psi}) \ . \qquad (10b)$$

The second term on the right hand side of each of these vanishes at the appropriate boundary of the problem space. Take these terms out by integrating them by parts.

Substituting (10) into (9) we obtain

$$\delta E[n(\vec{r})] = -\Re \iiint\limits_{space} [\frac{\partial \delta \psi}{\partial z} - \frac{i}{2k} \nabla_\perp^2 \delta \psi + \frac{i}{2k}(k^2 - k_0^2 n^2) \delta \psi] \tilde{\psi} \, d^3 r \ . \qquad (11)$$

The term in the brackets under the integral is most of (4): $\quad [\ ] = \frac{ik_0^2 n}{k} \psi \, \delta n \ .$

Substituting for the bracketed term we get

$$\delta E[n(\vec{r})] = -\Re \iiint\limits_{space} \frac{ik_0^2}{k} \psi(\vec{r})\tilde{\psi}(\vec{r})n(\vec{r})\delta n \, d^3 r$$

or

$$\delta E[n(\vec{r})] = \frac{k_0^2}{k} \Im \iiint\limits_{space} \psi(\vec{r})\tilde{\psi}(\vec{r})n(\vec{r})\delta n \, d^3 r \tag{12}$$

which, when we compare it to (3) yields a formula for the Fréchet derivative

$$\nabla_F E[n(\vec{r})] = \frac{k_0^2}{k} \Im[\psi(\vec{r})\tilde{\psi}(\vec{r})n(\vec{r})]$$

that we can use in optimization techniques such as steepest descent or conjugate gradient methods. In our case we have an index of refraction that includes attenuation, so we must make sure to use a complex n and δn in (12) which yields:

$$\nabla_F E[n] = \frac{k_0^2}{k}[\Re(\psi\tilde{\psi})(n_i\delta n_r + n_r\delta n_i) + \Im(\psi\tilde{\psi})(n_r\delta n_r - n_i\delta n_i)] \tag{13}$$

where n_i and n_r are the imaginary and real (attenuation and sound speed) parts of the complex index of refraction. This is the final form of the Fréchet derivative that we used in our reconstruction experiments.